Lasers in Manufacturing Conference 2023

In-situ monitoring of the laser powder bed fusion process by thermography, optical tomography and melt pool monitoring for defect detection

Nils Scheuschner[a,*], Frank Heinrichsdorff[b], Simon Oster[a], Eckart Uhlmann[c, d], Julian Polte[c, d], Anzhelika Gordei[c] , Kai Hilgenberg[a]

[a]*Bundesanstalt für Materialforschung und –prüfung (BAM), Unter den Eichen 87, 12205 Berlin, Germany*
[b]*Siemens AG, Siemensdamm 50, 13629 Berlin, Germany*
[c]*Fraunhofer-Institut für Produktionsanlagen und Konstruktionstechnik, Pascalstraße 8-9, 10587 Berlin, Germany*
[d]*Institut für Werkzeugmaschinen und Fabrikbetrieb (IWF), Technische Universität Berlin, Pascalstraße 8-9, 10587 Berlin, Germany*

Abstract

For the wide acceptance of the use of additive manufacturing (AM), it is required to provide reliable testing methods to ensure the safety of the additively manufactured parts. A possible solution could be the deployment of in-situ monitoring during the build process. However, for laser powder bed fusion using metal powders (PBF-LB/M) only a few in-situ monitoring techniques are commercially available (optical tomography, melt pool monitoring), which have not been researched to an extent that allows to guarantee the adherence to strict quality and safety standards.
In this contribution, we present results of a study of PBF-LB/M printed parts made of the nickel-based superalloy Haynes 282. The formation of defects was provoked by local variations of the process parameters and monitored by thermography, optical tomography and melt pool monitoring. Afterwards, the defects were characterized by computed tomography (CT) to identify the detection limits of the used in-situ techniques.

Keywords: Thermography; Optical tomography; Melt-pool-monitoring; Laser powder bed fusion; Haynes 282; Additive Manufacturing

* Corresponding author. Tel.: +49 30 8104 4260
E-mail address: nils.scheuschner@bam.de

1. Introduction

In-situ monitoring of additive manufacturing using nondestructive testing (NDT) methods is a very promising approach for quality control with many advantages over classic ex-situ NDT. Since the testing is carried out during the process, the total production time is not further extended by additional ex-situ NDT steps (Tapia and Alaa, 2014). Furthermore, for most AM processes the interior of the produced parts is directly accessible during production allowing to choose NDT methods like thermography and eddy current testing with low penetration depth, which would not be usable for ex-situ NDT in most cases (Ehlers *et al.*, 2022). Additionally, it is very conceivable that corrections, like additional exposure or a pause for cooling, could be performed to repair the part if the defect is detected in real time during the production (Feng *et al.*, 2022). Before in-situ monitoring can be used for quality control in a real production process a major challenge that has to be solved is understanding the in-situ monitoring signals and identifying the signatures of potential defects. In this work we examined three different in-situ monitoring techniques for PBF-LB/M: Thermography, optical tomography and coaxial mounted photodiodes (melt pool monitoring). The thermography and optical tomography setups were designed and implemented by us using commercially available components under the constraint that comparable systems covering the whole build plate should be implementable with reasonable development work and cost in a productive environment. By contrast the melt pool monitoring system was directly acquired from the manufacturer of the used PBF-LB/M machine. A challenge in researching in-situ monitoring for PBF-LB/M is the low defect rate of PBF-LB/M. Although many consider the PBF-LB/M process to produce many defects, the actual defect rate is typically too low to rely on statistically occurring defects especially considering the need to identify their occurrences by ex-situ testing. Therefore, we used local parameter variations to provoke defects. Creating specimen with artificial provoked defects by local parameter is a challenge. If the local parameter variations are too large it could lead to complete failure of the build job. If the local parameter variations are too small, the affected volumes can be completely remelted during processing the next layer. To verify the successful creation of defects in the specimen, X-ray computed tomography (XCT) was performed. Afterwards the in-situ monitoring data sets were analyzed for the actual created defects with the following two questions in mind: Does the monitoring system show signatures of the local parameter variations and are there signatures in the monitoring data for the following layers showing the presence of the defects while welding with the standard parameters?

2. Materials and methods

2.1. Material and L-PBF processing conditions

All experiments were carried out on a commercial PBF-LB/M single laser system SLM280 HL (SLM Solutions Group AG, Lübeck, Germany). The system was equipped with a 400-Watt continuous wave ytterbium fiber laser emitting at a wavelength of 1070 nm and a spot size of approximately 80 µm in focal position. All parts were manufactured on stainless steel substrate plates without platform preheating in an argon gas atmosphere with oxygen content below 0.1 %. To provide access for the off-axis optical in-situ monitoring, a sapphire window (Edmund Optics Inc., Barrington, USA) was integrated in the ceiling of the build chamber. To allow for an observation angle close to normal of the specimens, two gold mirrors were installed inside the build chamber. A schematic of the used setup can be found in Mohr *et al*., 2020. The total transmission and reflection losses from the window and the mirrors are estimated to be well below 10 % in the used wavelength ranges. The material used in the experiments is a commercial HAYNES® 282® superalloy powder. According to the supplier, it has an apparent density of 4.3 g cm^{-3} with the cumulative mass values d_{10} = 21.0 µm, d_{50} = 30.0 µm, d_{90} = 40.3 µm of the particle size distribution. HAYNES® 282® is a nickel based super alloy designed for

high temperature applications. The melting range of HAYNES® 282® is 1300 °C - 1375 °C. As the temperature strongly affects the intensity and spectrum of the thermal radiation, which is the quantity detected by all three used in-situ methods, care must be taken while using the results of this work for predictions for other materials.

2.2. Specimen geometry and scanning strategy

Six different cuboid shaped types of specimens with an outer hull dimension of (8 x 8 x 24) mm^3 were designed. For the layers without parameter variations, the laser power was set to 225 W with 1100 mm/s scanning velocity, 40 µm layer thickness and 100 µm hatch distance as scanning parameters. The scanning strategy was an alternating meander stripe pattern. All scan vectors were aligned parallel to the edges of the cuboids (without splitting into sections). After each layer the pattern was rotated by 90°. In each type of the specimen different local parameter variations were inserted. For specimen type 1, 2 and 3 the laser power, scanning velocity and hatch distance were variated for one to four neighboring scan vectors for 10 layers. The groups of modified scan vectors were separated by 1 mm (center to center) horizontally and 20 layers vertically. In specimen 4 the laser power was reduced six times for 10 whole successive layers separated by 20 layers with normal scanning parameters, followed by six times an increase of the scanning velocity for 10 layers (also separated by 20 layers). In specimen 5 the laser power was increased and the scanning velocity was reduced for 10 layers separated by 20 layers twelve times with normal scanning parameters. In specimen 6 unexposed volumes (cuboid shaped) were included in the geometry. Table 1 shows the range of the used parameter variations. Between the layers with parameter variations the rotation of the scanning pattern was suspended to allow a repetition of the local parameter variations under the exact same conditions. Each specimen type was marked on the top with a number ranging from 1 to 6. The upper right edge was slightly beveled for identifying the orientation. The specimens were rotated by 45° relatively to the shielding gas flow and the recoater moving direction on the base plate. Each parameter variation was at least repeated two times in each specimen testing for repeatability. Since optical tomography and thermography could not be used at the same time, the building process was repeated for both methods. Since the field of view for both methods was slightly different, the specimens were rearranged on the build plate for thermography.

Table 1. Used parameter variations

Specimen	Variation 1	Range in %	Size
1	Laserpower	60, 80, 90, 100, 110, 120, 140	1-4 vectors, 10 layers
2	Scanning velocity	60, 80, 90, 100, 110, 120, 140	1-4 vectors, 10 layers
3	Hatch distance	60, 80, 90, 100, 110, 120, 140	1-4 vectors, 10 layers
4	Laserpower or	65	10 layers, alternating
	Scanning velocity	150	
5	Laserpower and	177	10 layers
	Scanning velocity	66	
6	Pores/unexposed areas		length= 0.25, 0.5, 1.0 mm width = 1, 2, 4, 8 vectors height= 1, 2, 4, 8 layers

For six specimens, one of each type, XCT measurements and data analysis were commissioned (XPLORAYTION GmbH, Berlin, Germany). The XCT measurements were performed at the European Synchrotron Radiation Facility (BM18) with 140 keV average energy and a 2.62 mm molybdenum filter. The obtained XCT projection data was reconstructed, pre-processed and binarized into material and voids, resulting in a XCT data set with a resolution of (3.03 x 3.03 x 3.03) µm. Figure 1 shows the distribution of voids in specimen of type 3 and 6.

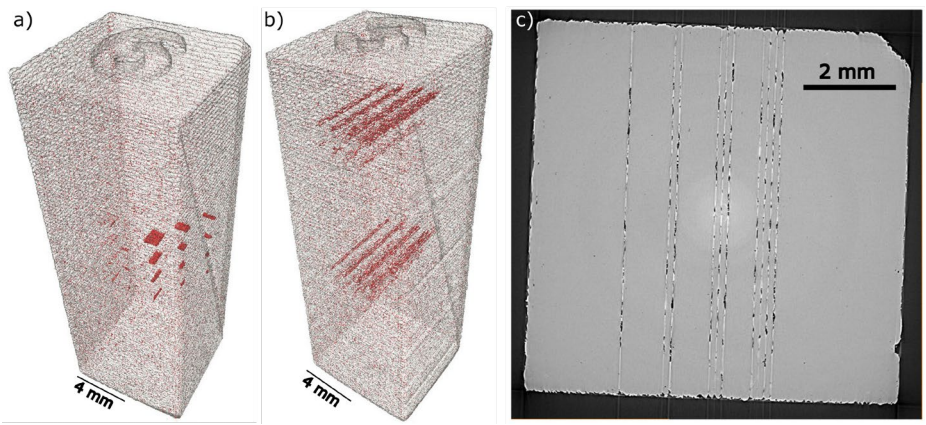

Fig.1. XCT reconstructions by XPLORAYTION GmbH: (a) and (b) Hull (gray) and voids (red) of specimen 6 and 3; (c) Cross-section of specimen 3 with 140 % hatch distance for 1-4 vectors.

For specimen 1 only the reduction to 60 % and 80 % laser power created a significant number of defects (voids) distributed statistically along the scan vectors. Changing the scanning velocity (specimen 2) had even less effect. Only for an increase to 140 % defects were observable. Changing the hatch distance (specimen 3) created defects for 120 % and 140 %. The parameter variations in specimen 4 and 5 created all statistically distributed defects in the corresponding segments, with a much higher density for the effective reductions of the volumetric energy density (VED) in specimen 4. For specimen 6 only the unexposed areas with 4- and 8-layers thickness were not remelted completely. For most unexposed volumes with 4-layers thickness only small pore areas around the contour remained in the final specimen while all 8-layers thick unexposed volumes created pores filled with unmolten metal powder but were smaller in all dimensions compared to the unexposed volumes.

2.3. Thermographic measurement set-up

For the thermographic measurement we used a shortwave IR-camera (C-Red 3, First Light Imaging SAS, Meyreuil, France) with a 50 mm objective IR-lens (LM50HC-IR, Kowa Optimed Deutschland GmbH), leading to a spatial resolution of 350 µm/px. The optical setup was protected from reflections of the process laser by a longpass filter (1150 nm). To increase to contribution of the lower temperature range to the total detected signal the detection range was limited to 1575 nm - 1625 nm with an additional bandpass filter. The field stop was set to f/4. To avoid overexposure a neutral density filter (ND 1.0) was used. The region of interest was set to 640 x 364 pixel allowing a frame rate of 841.76 Hz. The integration time was 1.182 ms leading to a semicontinuous monitoring of the process with only very short (~5 µs) interruptions during the read-out process. Due to the long integration time and the resulting motion blur, a thermographic calibration to determine the apparent temperatures was not possible. Instead, the raw intensity data is used for the analysis.

2.4. Optical tomography measurement set-up

For the optical tomography we used a monochromatic CMOS camera with 24.4 mega pixels and a pixel size of 2.74 µm x 2.74 µm (Basler ace 2 a2A5328-15um, Basler AG, Deutschland). As objective a 100 mm lens was used (COMPONON-S 5,6/100, Schneider-Kreuznach GmbH, Deutschland) leading to a spatial resolution of ~30 µm/px allowing to separate individual scan vectors. To avoid detecting radiation from atomic emission lines and to increase the contribution of the lower temperature range a 950 nm - 1000 nm bandpass filter was used. The exposure time was set to 10 s. From each raw frame a dark frame was subtracted to correct for the dark current. For each layer all corresponding frames were summed to create the final data set.

2.5. On-axis photodiodes measurement set-up (melt pool monitoring)

The integration of photodiodes into the beam path of the process laser by using at least one optical beam splitter is offered as an option from various PBF-LB/M machine manufacturers. For this study we used the commercial solution for the SLM280 HL called melt pool monitoring. Most technical details are undisclosed by the manufacturer. The system provides two signals from two different photodiodes for each datapoint. Since one of the signals is sensitive to the temperature of the substrate plate, it can be concluded that one diode must be more sensitive in the mid to far infrared region (~ 3-10 µm) while the other is more sensible to shorter wavelength (~1-3 µm). Furthermore, the use of an optical notch or long pass filter to protect the photodiodes from the process laser is extremely likely. While starting the data acquisition, it is possible to determine and correct for the dark stream of the photodiodes. The monitoring data is stored in a proprietary binary format but can be extracted as described by Schmid, 2018. Since the raw data is scattered (position and intensity data points), gridded data interpolation has been used to create the figures shown in this work.

3. Results and discussion

3.1. Optical Tomography

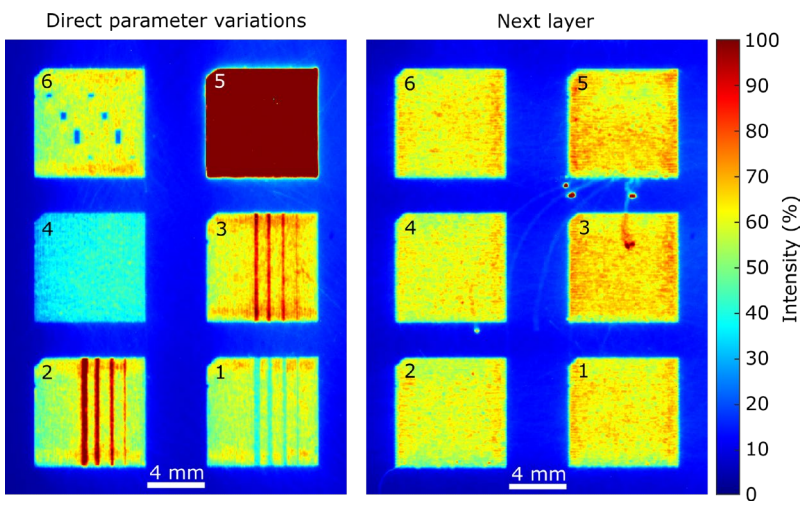

Fig. 2. Optical tomography showing all six types of specimens in a layer with parameter variation (left) and the next layer (right). The scale of the intensity was normalized to the dynamic range of the detector. For specimen 5 is the detector is saturated for the direct parameter variations.

Figure 2 shows two optical tomography images of subsequent layers, one layer with local parameter variations and the following using the standard scanning parameters. For the standard scanning parameters an intensity value in the range of 50 % - 70 % of the dynamic range of the camera was observed. Around the specimen an intensity value of ~25 % was observed caused by stray light. During processing the subsequent layer of specimen 5, large spatter particles have been emitted onto specimen 3 and the free area in between. Such events are very common but unlikely to cause defects. Nevertheless, such artefacts can be a huge challenge for automated assessment of optical tomography data. For all optical tomography measurements and all specimen no signatures for defects were found in the subsequent layers, whereas the local parameter variations can be clearly detected. For further analysis we have extracted the changes of the observed intensities for the 4-vectors width variation in specimen 1-3 relative to the intensity of the basis scanning parameter set, as a function of the change of the volumetric energy density (VED) (see Fig. 3). For all parameter variations the optical tomography intensity was nearly proportional to the VED.

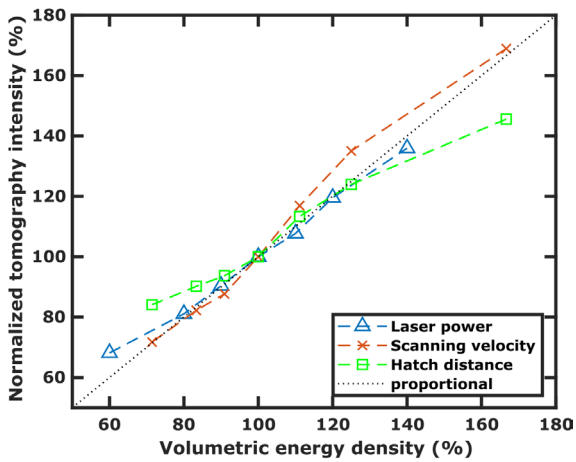

Fig. 3. Changes of the observed intensity of the optical tomography in the 4-vector wide local variations relative to a sound area with standard parameters as a function of the volumetric energy density relative to the standard parameters.

3.2. Melt Pool Monitoring

Figure 4 shows the melt pool monitoring data for the same layers and specimens as shown in Figure 3 for the optical tomography. Both MPM sensors show very similar results. For some areas with local parameter changes no data points were acquired (for instance specimen 1). This is most likely a software problem related to the parameter changes in the build file. For specimen 2 and 3 the vector with parameter changes were only very slightly contrasted relative to the normal scanning parameters and not well separable from the noise. For specimen 4 a reduction of the VED by 65% by increasing the scanning speed leads to only a very slight reduction of the signal for both sensors (~6800 vs. ~6850 counts for sensor 1 and ~17400 vs. ~17450 counts for sensor 2). Unfortunately the data points for the reduction of the VED by laser power in specimen 3 are missing. For specimen 5 the VED is in total increased to 270%. For both sensors the intensity increases in build direction over the specimen, it seems that quantitively the buildup of heat can be observed. For sensor 2 which we assume to be sensitive for longer wavelengths a slight increase in intensity in the subsequent layer is observable. Otherwise, there were no further indication of signatures of defects from previous layers in all acquired melt pool monitoring data.

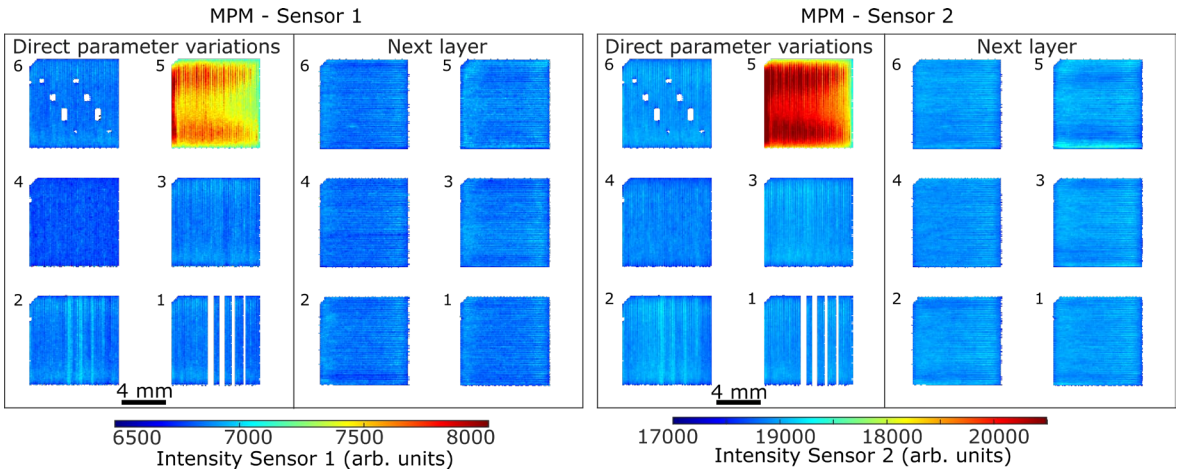

Fig. 4. Melt pool monitoring data showing all six types of specimens (black numbers) in a layer with parameter variation and the next layer. For specimen 1 the data points at the local parameter variations are missing.

3.3. Thermography

To analyze the thermographic raw data, it is necessary to reduce the 3D dataset to a 2D dataset. One straightforward approach is the integration of the signal at each point over the time for each layer which allows good comparability with optical tomography. Due to the large number of frames combined with noise, it is feasible to integrate only signals above a certain threshold value. For all further integrated thermography analysis, we choose this value to 100 counts (with an average maximum intensity for the basic scanning parameters of 3500 counts). Figure 5 shows the integrated thermography signal for a layer with parameter variations and for the next layer. Similar to the optical tomography the direct parameter variations are all directly noticeable, but with a lower spatial resolution. However, since the raw data of the thermography is resolved temporally, each scan vector could be separated for analysis if needed.

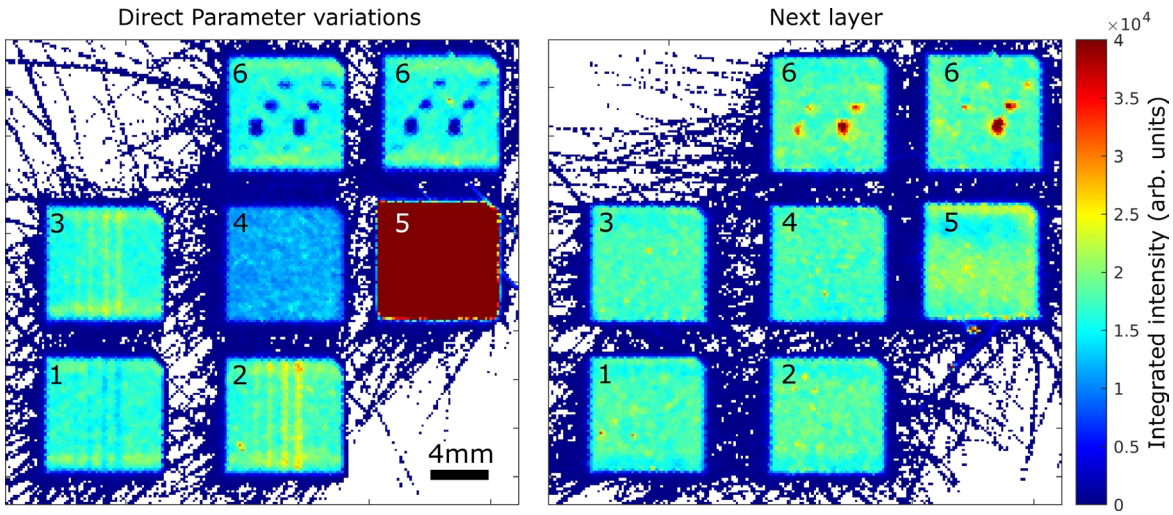

Fig. 5. (a) Integrated thermography in a layer with parameter variation (left) and the next layer (right). The signal of specimen 5 is not saturated for the direct parameter variations but lies outside the chosen intensity range. The specimen of the type 6 was produced two times in the same build job.

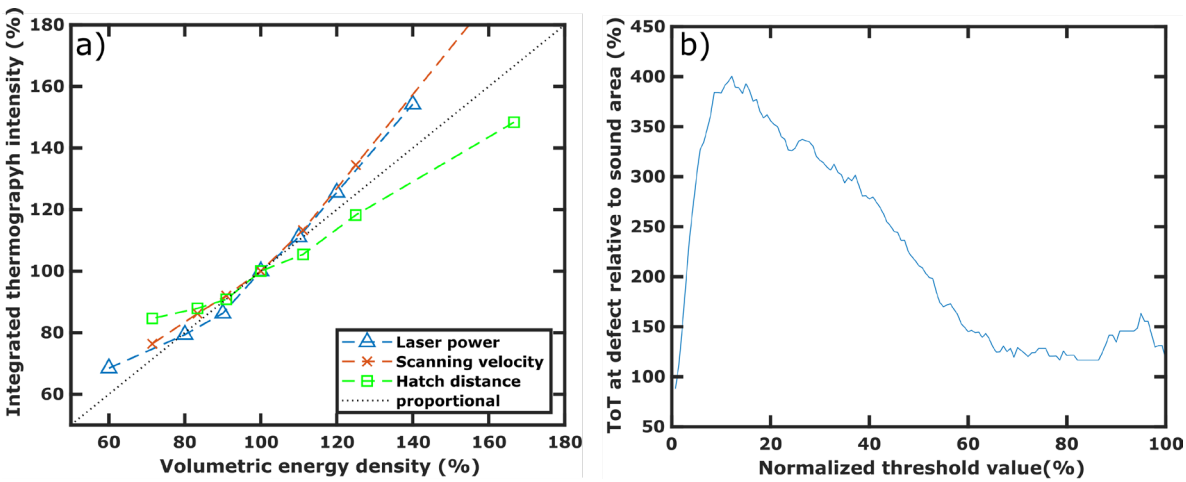

Fig. 6. (a) Integrated thermography intensity at the 4-vector wide local variations relative to a sound area as a function of the volumetric energy density relative to the standard parameters; (b) Time over threshold for the defect signature (largest pore) relative to a sound area as a function of the threshold value relative to the maximum of the raw thermographic data (standard parameters).

For further analysis we extracted the relative changes by the 4-vector wide local parameter variations as a function of the VED changes (see Fig. 6 (a)). The integrated thermography signal is in the examined VED range nearly proportional to the VED for all varied scanning parameters, also a non-linearity for the laser power and scanning speed as expectable from Planck's law is noticeable. This is confirmed by the results of specimen 4 where the VED reductions to 65% by laser power and scanning speed led both to a decrease of the integrated intensity to ~65%. Specimen 5 however confirms the non-linearity as an increase of the VED 270% leads to an increase of the integrated intensity to ~900%.

In the next layer pronounced signatures of defects can be found for the specimen of type 6. It appears that unmolten metal powder causes heat accumulations at the positions where pore defects were provoked in the previous layers. The signatures are more prominent for the pores on the right side which correlates to the thickness of the unexposed volumes (8 layers right, 4 layers left). To improve the analysis, we introduce the time over threshold (TOT) as an additional metric for the thermographic data (Altenburg *et al.*). The time over threshold is defined by the integral of the time when the intensity is above the selected threshold value. To find the optimal threshold value to maximize the defect signatures, we calculated the ratio of the time over threshold at the largest pore in specimen 6 relative to the time over threshold of a sound area as a function of the threshold (see Fig. 6(b)). From this analysis we selected a threshold value of 300 counts (8,6% of the mean maximum intensity) for the further analysis. The results of the time over threshold analysis for the next and after next layer are shown in Figure 7(b) and (c). Again, there are clear defect signatures in the next layer as well as there are defect signatures in the after next layer. For a qualitative analysis we extracted the maximal time over threshold values and integrated intensities above the pore areas relative to sound areas for all pore geometries with observable defect signatures in Table 2.

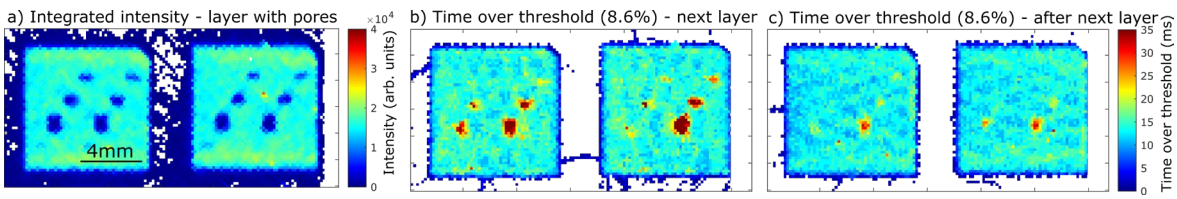

Fig. 7. (a) Integrated thermography intensity of the specimens of type 5 in a layer with parameter variation; (b) The time over threshold analysis of the following next layer; (c) and over next layer.

Table 2. Relative strength of the defect signature for different pore sizes (design parameters)

Pore width in mm	Pore length in mm	Pore thickness in mm	TOT (8.6 %) next layer in %	Integrated next layer in %	TOT (8.6 %) after next layer in %	Integrated after next layer in %
0.8	1.00	0.32	498	473	239	171
0.8	0.50	0.32	522	322	150	127
0.8	0.25	0.32	185	154	124	119
0.4	1.00	0.32	187	171	205	140
0.4	0.50	0.32	171	127	134	108
0.4	0.25	0.32	163	119	134	107
0.8	1.00	0.16	450	319	239	168
0.8	0.50	0.16	273	199	168	146
0.8	0.25	0.16	145	121	150	119

The standard deviation of the integrated intensity (time over threshold) in the sound area is 7 % (11 %). With five sigma significance all pore geometries with more than 135 % integrated intensity or 155 % time over threshold should be detectable under the assumption that the defect signatures magnitudes are quite constant. Furthermore, since the defect signatures extend over several neighboring pixels, the sensitivity could be increase further by averaging spatially on cost of the spatial resolution. Therefore it is quite safe to assume

that all pores in Table 2 with defect signature >180 % can reliably be detected by thermography, also this must be verified by a statically relevant follow up experiment.

4. Conclusions

Three optical in-situ monitoring methods (optical tomography, thermography and melt pool monitoring) for PBF-LB/M were examined. While optical tomography is the least technically challenging method, it was only capable to monitor the direct parameter changes introduced to provoke artificial defects in the specimen. Furthermore, it showed to be sensitive to spatter which could lead to false positives for fully automated analysis. Melt pool monitoring (and thermography) seems to be the more robust and less problematic in this regard. However, it was very hard to detect even the direct parameter changes in the MPM data. Due to missing data points and due to the undisclosed technical details, it is not possible to draw a final conclusion onto the useability of MPM as in-situ monitoring technique for the detection of defects. From all three presented methods thermography showed the most promising results. The integrated thermography signal showed signatures for all local parameter variations and could be correlated to the VED. For higher frame rates and spatial resolutions as used in this work, it would also be possible to determine the apparent temperatures of the melt pool by thermography. Thermography was the only method that showed defect signatures in the following layers after provoking the defects. Pores filled with unmolten powder caused by unexposed volumes >= (0.8 x 0.5 x 0.32) mm^3 could very reliably be detected by sensing the heat accumulation in the next layer.

Acknowledgements

The authors would like to thank Toni Räpke (BAM) for providing the used scanning parameters. This research work was carried out within the *Werner-von-Siemens Centre for Industry and Science* in the *HTA 2.0 - High Temperature Applications* project, co-funded by the European Regional Development Fund (ERDF).

References

Altenburg S., Scheuschner N., Maierhofer C., Mohr G., Hilgenberg K., 2020, Thermography in laser powder bed fusion of metals: time over threshold as feasible feature in thermographic data, Proceedings of Conference QIRT 2020, doi:10.21611/qirt.2020.005

Ehlers H.,Thewes R., Pelkner M., 2022, Online Process Monitoring for Additive Manufacturing Using Eddy Current Testing With Magnetoresistive Sensor Arrays, IEEE Sensors Journal, VOL. 22, NO. 20, doi:10.1109/JSEN.2022.3205177

Feng, S., Chen Z., Bircher B., Ji Z., Nyborg L., Bigot S, 2022, Predicting Laser Powder Bed Fusion Defects through in-Process Monitoring Data and Machine Learning. Materials & Design 222, doi:10.1016/j.matdes.2022.111115

Mohr G., Scheuschner N, Hilgenberg K., 2020, In situ heat accumulation by geometrical features obstructing heat flux and by reduced inter layer times in laser powder bed fusion of AISI 316L stainless steel, Procedia CIRP, doi:10.1016/j.procir.2020.09.030

Schmid S, 2018, Detektion von Prozessstörungen beim Laserstrahlschmelzen mittels Online-Prozessüberwachung und Methoden des maschinellen Lernens, Semesterarbeit, https://mediatum.ub.tum.de/1462525

Tapia, G., Alaa E., 2014, A Review on Process Monitoring and Control in Metal-Based Additive Manufacturing, Journal of Manufacturing Science and Engineering 136, doi:10.1115/1.4028540.